

This item is likely protected under Title 17 of the U.S. Copyright Law. Unless on a Creative Commons license, for uses protected by Copyright Law, contact the copyright holder or the author.

Access to this work was provided by the University of Maryland, Baltimore County (UMBC) ScholarWorks@UMBC digital repository on the Maryland Shared Open Access (MD-SOAR) platform.

Please provide feedback

Please support the ScholarWorks@UMBC repository by emailing scholarworks-group@umbc.edu and telling us what having access to this work means to you and why it's important to you. Thank you.

A COMPREHENSIVE SPECTRAL ANALYSIS OF THE X-RAY PULSAR 4U 1907+09 FROM TWO OBSERVATIONS WITH THE *SUZAKU* X-RAY OBSERVATORY

ELIZABETH RIVERS¹, ALEX MARKOWITZ¹, KATJA POTTSCHMIDT^{2,3}, STEFANIE ROTH⁴, LAURA BARRAGÁN⁴, FELIX FÜRST⁴,
SLAWOMIR SUCHY¹, INGO KREYKENBOHM⁴, JÖRN WILMS⁴, AND RICHARD ROTHSCHILD¹

¹ Center for Astrophysics and Space Sciences, University of California, San Diego, 9500 Gilman Dr., La Jolla, CA 92093-0424, USA; erivers@ucsd.edu

² CRESST and NASA Goddard Space Flight Center, Astrophysics Science Division, Code 661, Greenbelt, MD 20771, USA

³ Center for Space Science and Technology, University of Maryland, Baltimore County, 1000 Hilltop Circle, Baltimore, MD 21250, USA

⁴ Dr. Karl-Remeis-Sternwarte and Erlangen Centre for Astroparticle Physics, Sternwartstr. 7, 96049 Bamberg, Germany

Received 2009 August 25; accepted 2009 December 1; published 2009 December 29

ABSTRACT

We present results from two observations of the wind-accreting X-ray pulsar 4U 1907+09 using the *Suzaku* Observatory. The broadband time-averaged spectrum allows us to examine the continuum emission of the source and the cyclotron resonance scattering feature at ~ 19 keV. Additionally, using the narrow CCD response of *Suzaku* near 6 keV allows us to study in detail the Fe K bandpass and to quantify the Fe K β line for this source for the first time. The source is absorbed by fully covering material along the line of sight with a column density of $N_{\text{H}} \sim 2 \times 10^{22} \text{ cm}^{-2}$, consistent with a wind-accreting geometry, and a high Fe abundance (~ 3 – 4 times solar). Time- and phase-resolved analyses allow us to study variations in the source spectrum. In particular, dips found in the 2006 observation which are consistent with earlier observations occur in the hard X-ray bandpass, implying a variation of the whole continuum rather than occultation by intervening material, while a dip near the end of the 2007 observation occurs mainly in the lower energies implying an increase in N_{H} along the line of sight, perhaps indicating clumpiness in the stellar wind.

Key words: pulsars: individual (4U 1907+09) – stars: magnetic field – X-rays: binaries – X-rays: stars

Online-only material: color figures

1. INTRODUCTION

Discovered by Giacconi et al. (1971), the X-ray pulsar 4U 1907+09 is a wind-accreting high-mass X-ray binary (HMXB) with a highly reddened companion star of magnitude $m_{\text{bol}} = 16.37$ mag, luminosity $L_{\text{bol}} = 5 \times 10^5 L_{\odot}$, and a mass loss rate of $\dot{M} = 7 \times 10^{-6} M_{\odot} \text{ yr}^{-1}$ (Cox et al. 2005). The neutron star is in an eccentric orbit with a period of 8.3753 days. Orbital parameters can be found in in’t Zand et al. (1998).

From 1983, when Makishima et al. (1984) found the source to have pulsations, through 1998, the pulse period had a steady spin-down rate of $\dot{P}_{\text{pulse}} = +0.225 \text{ s yr}^{-1}$, going from 437.5 s to 440.3 s (in’t Zand et al. 1998). Baykal et al. (2006) reported a deviation from the spin-down rate, measuring a much lower value between 1998 and 2003, which in 2002 was half the long-term value ($\sim 0.115 \text{ s yr}^{-1}$). Using *INTEGRAL* data, Fritz et al. (2006) demonstrated that between 2004 and 2005 a complete torque reversal occurred with a maximum period of ~ 441.3 s being reached in 2004 April followed by spin-up behavior with $\dot{P}_{\text{pulse}} = -0.158 \pm 0.007 \text{ s yr}^{-1}$. Inam et al. (2009), using *Rossi X-Ray Timing Explorer* (*RXTE*)-PCA data between 2007 and 2008, reported a second torque reversal and a new spin-down rate of $+0.220 \text{ s yr}^{-1}$, consistent with the rate before 1998.

Using data from *Ginga* observations of 4U 1907+09, Makishima et al. (1992, 1999) reported a cyclotron resonance scattering feature (CRSF) at ~ 19 keV. CRSFs or “cyclotron lines” are generated by photons scattering on electrons in the strong magnetic field near the surface of a neutron star. Photons from the accretion column above the magnetic poles that are near the energies that separate the Landau levels of the electrons are scattered out of the line of sight, the effect resembling an absorption line (see, e.g., Nagel 1981; Schönherr et al. 2007 for details). These features can thus be used to directly measure

the magnetic field strength of the pulsar. Using *BeppoSAX* observations, Cusumano et al. (1998) later confirmed the CRSF for 4U 1907+09 at ~ 19 keV and calculated a strong surface magnetic field of $2.1 \times 10^{12} \text{ G}$. Cusumano et al. also reported a harmonic at ~ 39 keV and an iron emission line near 6.4 keV with an equivalent width of about 60 eV.

4U 1907+09 was discovered to have an orbital period of 8.38 days by Marshall & Ricketts (1980) and to display periodic flaring behavior over the orbit as well as occasional dipping behavior. The flaring was originally believed to be due to a Be-type companion star, where the flares corresponded to the neutron star passing through the companion’s outer atmosphere. Van Kerkwijk et al. (1989), however, optically identified the companion star 4U 1907+097 as a supergiant, contradicting the earlier assumption. This was later confirmed by Cox et al. (2005) who identified the companion as a type O8/O9 supergiant with a dense stellar wind, leading to the current belief that the pulsar is entirely wind-accreting.

The dipping behavior has been observed, notably by the *RXTE*, as reductions in intensity for periods on the scale of 1 hr, occasionally dropping completely below detection levels (in’t Zand et al. 1997). Due to the absence of strong variations in the column density, the lack of correlation with the orbital phase, and various spectral features, in’t Zand et al. have suggested that these dips are due to the cessation of mass accretion rather than occultation of intervening material.

In this paper, we present data from the Japanese X-ray Observatory *Suzaku* which observed the source twice, in 2006 and 2007. In Section 2, we describe the instruments and the data reduction process. In Section 3, we describe our methods and results for time-averaged spectral fitting, including details of the 6.4 keV iron emission line and the CRSF at 19 keV. Section 4 shows the results of pulse-period determination and

phase-resolved spectral fitting. In Section 5, we detail time-resolved spectral fitting in order to explore the dipping behavior seen in both observations and the flaring seen in the 2007 observation. Sections 6 and 7 are devoted to a detailed discussion and a summary of our conclusions, respectively.

2. DATA REDUCTION AND ANALYSIS

Suzaku observed 4U 1907+09 with the X-ray Imaging Spectrometer (XIS; Mitsuda et al. 2007) and the Hard X-ray Detector (HXD; Takahashi et al. 2007) beginning 2006 May 2 at 06:11 UT (MJD 53857.3) for 123 ks and again 2007 April 19 starting at 10:03 UT (MJD 54209.4) for 158 ks. The observation IDs are 401057010 and 402067010, respectively. The HXD gathered data with both its detectors, the PIN diodes and the GSO scintillators; however, we did not use the GSO data because of the faintness of the source in the GSO band relative to the non-X-ray background (NXB). The XIS has four CCDs: 0–3 with 0, 2, and 3 front-illuminated, and XIS1 back-illuminated. In November of 2006, XIS2 was damaged and taken off-line; therefore data in the 2007 observation were taken with only the remaining three XISs. Two corners of each XIS CCD have an ^{55}Fe calibration source which can be used to calibrate the gain and test the spectral resolution of data taken using this instrument (see the *Suzaku* Data Reduction Guide⁵ for details).

During the 2006 observation the XIS was set to 1/4 window mode to avoid saturating the CCDs should the flux during the source’s flares have proven to be too high. However, this did not prove to be the case and for the 2007 observation the mode was switched to full window. The pointing was also changed from XIS nominal pointing in 2006 to HXD nominal, both to reduce the flux in the XIS by a small fraction (10%) and to increase the sensitivity above 12 keV for analysis of the CRSF.

Data were processed with version 2.0.6.13 of the *Suzaku* pipeline and screened to exclude data within 436 s of passing through the South Atlantic Anomaly and within Earth elevation angles of less than 5° or Bright Earth angles of less than 20° . All extractions were done using HEASOFT v.6.6.2.

2.1. XIS Reduction

After screening, the good exposure time per XIS was 58.4 ks for 2006 and 80.6 ks for 2007. The XIS CCDs were in the 3×3 and 5×5 editing modes which were cleaned and added to create image files for each XIS. Data from each CCD were analyzed separately. From these we extracted source and background light curves and spectra and used XISRMFGEN and XISSIMARFGEN to create the response matrix (RMF) and ancillary response (ARF) files. There was no charge injection in either observation. Channels were grouped by 5 channels below 1.5 keV and 10 channels from 1.5–10 keV. Data below 1 keV and above 10 keV were ignored for all XISs in both observations, due to complete absorption below 1 keV and instrument noise above 10 keV. In addition, data between 1.8 and 2.7 keV and between 1.65 and 2.3 keV were ignored for the 2006 and 2007 observations respectively, due to poorly understood calibration for the Si K complex and Au M edge arising from the detector and mirror system.

Fitting the ^{55}Fe calibration sources for 2007 in XSPEC v.11.3.2ag (Arnaud 1996) with a model comprised of three Gaussian components (Mn $K\alpha_1$, $K\alpha_2$, and $K\beta$) yielded the

following results for the Mn $K\alpha_1$ line energy (expected value of 5.899 keV): 5.829 ± 0.004 keV for XIS0, 5.886 ± 0.006 keV for XIS1, and 5.920 ± 0.007 keV for XIS3, showing that the energy calibration is good to 20 eV in XIS1 and XIS3 and to 70 eV in XIS0. No calibration spectra were available for the 2006 data which were in 1/4 window mode, and therefore did not see the corners of the CCDs.

2.2. PIN Reduction

The *Suzaku* HXD/PIN is a non-imaging instrument with a $34'$ square (FWHM) field of view. The HXD instrument team provides NXB event files using the calibrated GSO data for the particle background monitor (“background D” or “tuned background” with METHOD=LCFITDT). This yields instrument backgrounds with $\lesssim 1.5\%$ systematic uncertainty at the 1σ level (Fukazawa et al. 2009). As suggested in the *Suzaku* ABC Guide, the cosmic X-ray background was simulated in XSPEC v.11 using the form of Boldt (1987).

Net spectra were extracted and deadtime-corrected for a net exposure time of 32.0 ks for 2006 and 64.9 ks for 2007. We excluded PIN data below 13 keV due to thermal noise. In both observations, the source flux falls to levels well below a few percent of the background at ~ 40 keV for our time-averaged spectra, and therefore we only use data between 13 and 40 keV. Channels were grouped with a minimum of 50 counts per bin to allow χ^2 fitting.

3. TIME-AVERAGED SPECTRAL ANALYSIS

All spectral fitting in this paper used XSPEC v.11.3.2ag (Arnaud 1996). Unless otherwise stated, all uncertainties below correspond to $\Delta\chi^2 = 2.71$ (90% confidence level for one parameter). For the time-averaged fits the normalization for XIS0 was fixed while the cross-normalizations were left free for XIS1, 2, and 3 (2006) and for XIS1 and 3 (2007); best-fit values of χ^2/dof were usually close to unity. The PIN/XIS0 cross-normalization was set to 1.16 (2006, XIS-nominal) or 1.18 (2007, HXD-nominal pointing; Maeda et al. 2008). Allowing the cross-normalization to be free resulted in unrealistic values due to a broad feature around 8–15 keV. We fit the XIS+PIN data in the range 1–40 keV. The 2006 data are shown in Figure 1(a); the 2007 data are shown in Figure 2(a).

Our initial continuum model consisted of a power-law continuum emission component with a high-energy rollover, plus full-covering absorption by a cold column of gas along the line of sight. For both the 2006 and 2007 observations, we considered three forms for the power-law continuum rollover: a power law with a smooth Fermi–Dirac cutoff “FDCut” (Tanaka 1986), a power law with an abrupt exponential cutoff, “HighECut” (White et al. 1983), and the “NPEX” model consisting of negative and positive power laws with a common exponential cutoff (Mihara 1995). Qualitatively, all models gave similar overall results for each observation. For the purposes of this paper, we will be using the FDCut model to illustrate how spectral fitting proceeded and to fit the time- and phase-resolved spectra. We include the other two models as an alternate phenomenological descriptions of the continuum and for ease of comparison with other observations.

For the absorber, we assumed the elemental abundances of Wilms et al. (2000) and the photo-absorption cross sections of Verner et al. (1996); solar abundances were initially assumed. Data/model ratios to this best-fit initial FDCut model are shown in Figures 1(b) and 2(b) for 2006 and 2007, respectively. Initial

⁵ <http://heasarc.gsfc.nasa.gov/docs/suzaku/analysis/abc/abc.html>

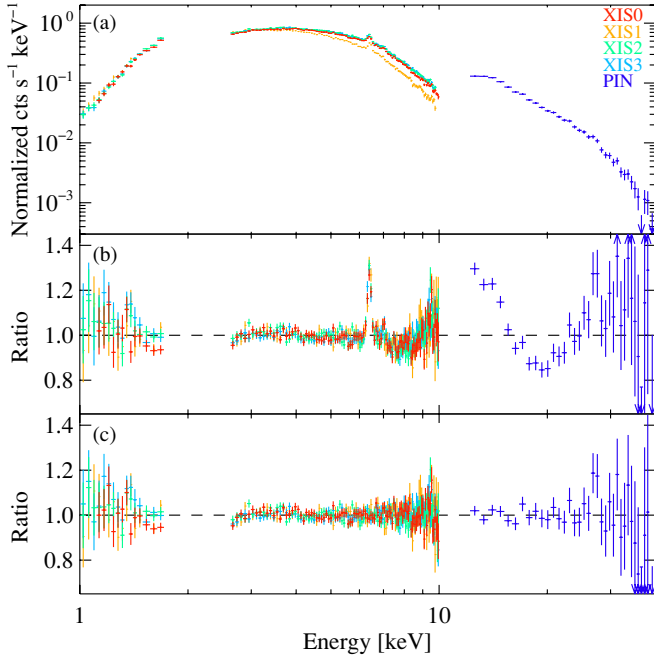


Figure 1. Time-averaged spectral fitting for 2006. Panel (a) shows the data, all four XISs, and the PIN. Panel (b) shows the data/model residuals for an absorbed continuum model with FDCut. Panel (c) shows the data/model ratios for our best-fit model including the iron lines, 10 keV feature, and the CRSF. (A color version of this figure is available in the online journal.)

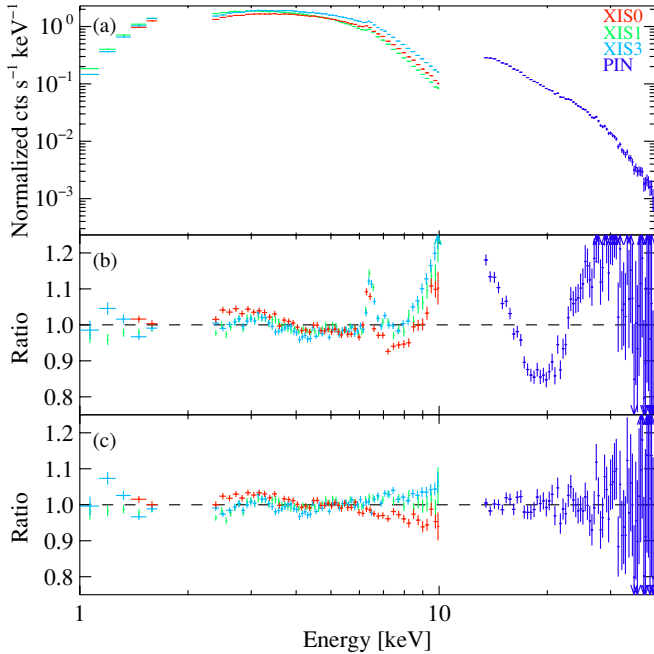


Figure 2. Time-averaged spectral fitting for 2007. Panel (a) shows the data, three XISs, and the PIN. Panel (b) shows the data/model residuals for an absorbed continuum model with FDCut. Panel (c) shows the data/model ratios for our best-fit model including the iron lines, 10 keV feature, and the CRSF. (A color version of this figure is available in the online journal.)

values for χ^2/dof were 2689.41/996 (2006) and 3820.61/784 (2007).

Figures 3 and 4 show the data/model ratios in the Fe K bandpass. Both spectra showed narrow, positive data/model residuals at 6.4 keV, evidence for the Fe K α emission line. We modeled this line using a Gaussian component. In the 2007

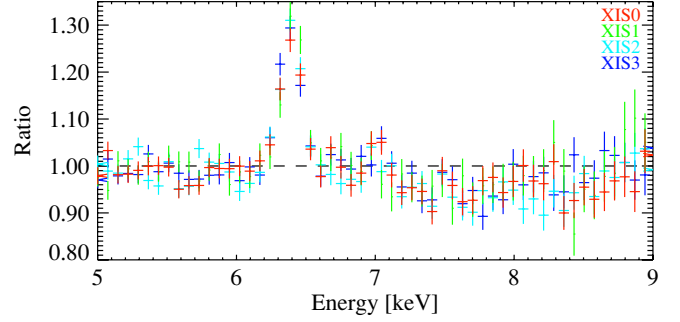


Figure 3. Data/model residuals focusing on the iron K bandpass for 2006 when the continuum is modeled as in Figure 1(b). (A color version of this figure is available in the online journal.)

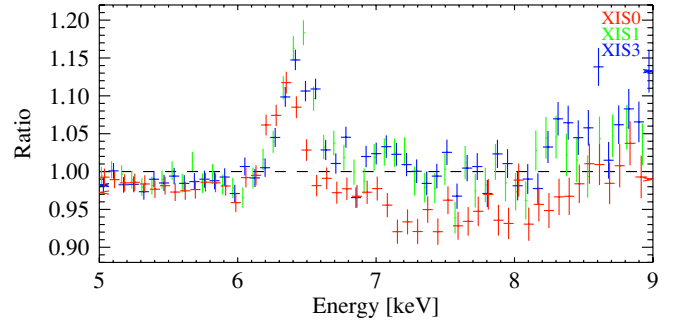


Figure 4. Data/model residuals focusing on the iron K bandpass for 2007 when the continuum is modeled as in Figure 2(b). (A color version of this figure is available in the online journal.)

fit, we allowed the line energy to be free for all three XISs based on the differences in gain observed in the calibration source. This allowed for a much better fit of the K α line in the 2007 data. It was not necessary to do this in the 2006 data.

Strong data/model ratios near ~ 15 – 25 keV (Figures 1(b) and 2(b)) indicated the presence of the CRSF, which we modeled using a Gaussian component in absorption. The actual shape of the CRSF is more complicated, but for the purposes of fitting, a Gaussian is adequate to model the feature (Schönherr et al. 2007). In our best-fit model, the Gaussian centroid energy was $18.6^{+0.8}_{-0.7}$ keV (2006) and 19.1 ± 0.2 keV (2007), consistent with previous results by Cusumano et al. (1998) and Makishima et al. (1992, 1999); note that Makishima et al. used a Lorentzian line profile while we and Cusumano et al. used a Gaussian; however, the two profiles have similar energy centroids despite their different shapes. We were not able to search for the second harmonic at ~ 39 keV since the PIN spectrum becomes background dominated in that region.

We modeled positive ratios above 8 keV in the XIS and below ~ 15 keV in the PIN with a broad emission feature peaking around 10–13 keV. The “10 keV” bump feature has been observed previously in this source by Mihara (1995) and Coburn et al. (2002) as well as in several other cyclotron line sources, e.g., with *RXTE* in MXB 0656–072 (McBride et al. 2006), Her X-1, 4U 1626–67, and 4U 1538–52 (Coburn et al. 2002), and Cen X-3 (Suchy et al. 2008); and with *Ginga* in 4U 1538–52 and V 0331+53 (Mihara 1995). Though the physical nature of this feature is still not clear, it cannot stem from calibration issues since it has been seen with multiple satellites. It is believed to be part of the overall continuum and including this feature as a broad Gaussian emission component in the model is required for a good fit. χ^2/dof fell from 1660.25/990 to 1125.39/987 (2006) and from 1743.56/776 to 1315.54/773 (2007).

Table 1
Time-averaged Spectral Fit Parameters

Model Parameter	FDCut		HighECut		NPEX	
	2006	2007	2006	2007	2006	2007
2–10 keV flux (erg cm ⁻² s ⁻¹)	1.5×10^{-10}	3.8×10^{-10}
N_{H} (10 ²² cm ⁻²)	$2.9^{+0.1}_{-0.1}$	$2.5^{+0.2}_{-0.2}$	$3.0^{+0.3}_{-0.2}$	$2.3^{+0.2}_{-0.2}$	$2.7^{+0.1}_{-0.1}$	$2.2^{+0.1}_{-0.1}$
Fe abundance (rel. to solar)	$3.9^{+0.9}_{-0.7}$	$3.0^{+1.0}_{-0.6}$	$2.8^{+0.6}_{-0.7}$	$3.6^{+0.1}_{-0.1}$	$3.6^{+1.0}_{-0.8}$	$3.3^{+0.6}_{-0.5}$
Photon index	$1.08^{+0.02}_{-0.02}$	$1.21^{+0.01}_{-0.01}$	$1.09^{+0.03}_{-0.04}$	$1.25^{+0.01}_{-0.01}$
Power-law norm ^a	$2.36^{+0.07}_{-0.06} \times 10^{-2}$	$5.07^{+0.04}_{-0.04} \times 10^{-2}$	$1.85^{+0.07}_{-0.06} \times 10^{-2}$	$5.07^{+0.04}_{-0.04} \times 10^{-2}$
Cutoff energy (keV)	$13.6^{+1.3}_{-1.3}$	$22.6^{+0.3}_{-0.3}$	$20.4^{+2.9}_{-1.8}$	$20.7^{+0.2}_{-0.2}$
Folding energy (keV)	$9.5^{+0.4}_{-0.4}$	$6.4^{+0.2}_{-0.2}$	$6.6^{+1.0}_{-1.0}$	$7.1^{+0.2}_{-0.2}$
NPEX $\alpha 1$	$0.56^{+0.03}_{-0.02}$	$0.65^{+0.01}_{-0.01}$
NPEX $\alpha 2$	–2.00 (fixed)	–2.00 (fixed)
NPEX norm 1 (10 ⁻²)	$1.73^{+0.10}_{-0.07}$	$4.73^{+0.08}_{-0.08}$
NPEX norm 2 (10 ⁻³)	$2.5^{+1.0}_{-0.3}$	$3.3^{+0.1}_{-0.1}$
NPEX temperature (keV)	$4.9^{+0.1}_{-0.3}$	$4.53^{+0.01}_{-0.01}$
CRSF energy (keV)	$18.6^{+0.8}_{-0.7}$	$19.3^{+0.2}_{-0.2}$	18^{+3}_{-1}	$19.9^{+0.7}_{-0.7}$	$18.4^{+1.0}_{-1.8}$	$19.1^{+0.2}_{-0.2}$
CRSF σ (keV)	$2.0^{+1.2}_{-0.9}$	$2.8^{+0.3}_{-0.3}$	$5.8^{+1.6}_{-0.8}$	$3.2^{+0.4}_{-0.4}$	$3.6^{+1.7}_{-1.1}$	$2.7^{+0.2}_{-0.2}$
CRSF depth	$0.21^{+0.10}_{-0.06}$	$0.41^{+0.03}_{-0.03}$	$1.0^{+0.1}_{-0.1}$	$0.78^{+0.05}_{-0.08}$	$0.30^{+0.09}_{-0.05}$	$0.47^{+0.01}_{-0.03}$
10 keV bump energy (keV)	$12.2^{+1.2}_{-0.2}$	$11.4^{+0.1}_{-0.1}$	$12.8^{+0.3}_{-0.2}$	$11.3^{+0.1}_{-0.1}$	$12.3^{+0.4}_{-0.4}$	$11.2^{+0.1}_{-0.1}$
10 keV bump σ (keV)	$1.5^{+0.1}_{-0.2}$	$1.9^{+0.2}_{-0.2}$	$2.1^{+0.2}_{-0.2}$	$1.4^{+0.2}_{-0.2}$	$1.5^{+0.4}_{-0.3}$	$1.3^{+0.2}_{-0.2}$
10 keV bump intensity ^b	$3.2^{+0.5}_{-0.4} \times 10^{-3}$	$3.8^{+0.3}_{-0.3} \times 10^{-3}$	$5.7^{+1.8}_{-1.5} \times 10^{-3}$	$2.5^{+0.2}_{-0.2} \times 10^{-3}$	$1.8^{+1.8}_{-0.5} \times 10^{-3}$	$2.3^{+0.3}_{-0.3} \times 10^{-3}$
Fe K α line energy (keV)	$6.394^{+0.005}_{-0.005}$	$6.41^{+0.02}_{-0.02}$	$6.394^{+0.005}_{-0.005}$	$6.43^{+0.02}_{-0.02}$	$6.394^{+0.005}_{-0.005}$	$6.43^{+0.02}_{-0.02}$
Fe K α line σ (eV)	< 35	68^{+9}_{-21}	30^{+10}_{-16}	66^{+14}_{-16}	28^{+16}_{-10}	71^{+15}_{-15}
Fe K α line intensity ^b	$2.0^{+0.1}_{-0.1} \times 10^{-4}$	$2.5^{+0.2}_{-0.2} \times 10^{-4}$	$1.6^{+0.1}_{-0.1} \times 10^{-4}$	$2.3^{+0.2}_{-0.2} \times 10^{-4}$	$1.4^{+0.1}_{-0.1} \times 10^{-4}$	$2.4^{+0.2}_{-0.2} \times 10^{-4}$
Fe K α line equivalent width (eV)	62 ± 3	47 ± 4	67 ± 4	46 ± 4	65 ± 4	48 ± 4
Fe K β line energy (keV)	$7.03^{+0.04}_{-0.04}$	$7.0^{+0.1}_{-0.1}$	$7.02^{+0.04}_{-0.04}$	$7.1^{+0.1}_{-0.1}$	$7.02^{+0.04}_{-0.04}$	$7.0^{+0.1}_{-0.1}$
χ^2/dof	1040.19/985	1239.02/766	1036.78/985	1248.23/766	1018.14/985	1213.07/766
Reduced χ^2	1.06	1.62	1.05	1.63	1.03	1.59

Notes.

^a Units are ph keV⁻¹ cm⁻² s⁻¹ at 1 keV.

^b Units are ph cm⁻² s⁻¹.

The best-fit energy centroid for this component falls within or close to the gap in energy coverage between the XIS and PIN and the effective areas of the XIS and PIN are low in this region. The energy, width, and intensity of this component as derived with *Suzaku* may therefore be affected by systematic uncertainties which are difficult to quantify.

Next, we noticed narrow positive data/model ratios near 7.1 keV, seen in all four XISs in 2006 and primarily in XIS1 and 3 in 2007. We identify this feature as Fe K β emission; detection of this line in 4U 1907+09 is reported here for the first time. Modeling it with a Gaussian component, with the energy left as a free parameter and the width of the K β line kept tied to that of the K α line, χ^2/dof fell to 1090.11/986 (2006) or 1290.08/770 (2007). In our best-fit model, it was significant at the 99.994% (2006) or 99.998% (2007) confidence level to include this component according to an *F*-test (which formally cannot be used in this manner due to a boundary condition violation as per Protassov et al. 2002, but can give a rough approximation of the significance). The best-fit value of the intensity was $13\% \pm 5\%$ that of the K α line, consistent with an origin in neutral or at most moderately ionized (< XIII) species of Fe (Palmeri et al. 2003). For the remainder of this paper, the K β normalization is fixed to 13% that of the K α line.

Finally, we noticed absorption-like data/model ratios between 7 and 8 keV. We fit this edge-like feature by allowing the Fe abundance of the absorber relative to solar, Z_{Fe} , to vary.

As shown in Table 1, values of Z_{Fe} near 3–4 were typically obtained. We thus obtained our best-fit model, with χ^2/dof falling to 1040.19/985 (2006) or 1239.02/766 (2007). This edge is consistent with our values for the Fe K α and K β lines, all of which have significant physical implications as will be discussed in Section 6.3.

Figures 1(c) and 2(c) show the data/model ratios for our best-fit FDCut models, with all the above-mentioned components included. Best-fit model parameters are listed in Table 1 for the FDCut, HighECut, and NPEX fits to the 2006 and 2007 spectra. Flux values for the two observations were 1.5 and 2.8×10^{-10} erg cm⁻² s⁻¹. These fits are robust to $\pm 2\%$ variations in the PIN background level (Fukazawa et al. 2009).

4. PHASE-RESOLVED SPECTROSCOPY

4.1. Pulse-period Determination

To measure the pulse period, we performed epoch folding (Leahy et al. 1983) on the PIN data for each observation, excluding the gaps due to the satellite orbit and only using the first ~ 50 ks for the 2006 observation to avoid the pronounced dip beginning midway through that observation. The 2006 observation pulse period was found to be 441.09 ± 0.05 s while the 2007 observation pulse period was found to be 441.03 ± 0.03 s. Uncertainties are due to strong pulse-to-pulse variations as well as the brevity of our observations compared to

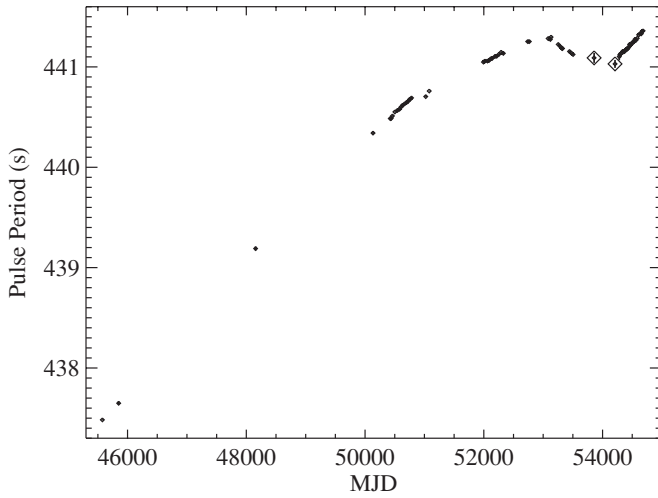


Figure 5. Pulse-period evolution from 1983 to 2008, using data from Baykal et al. (2001, 2006), Fritz et al. (2006), Inam et al. (2009), and this work (indicated by diamonds).

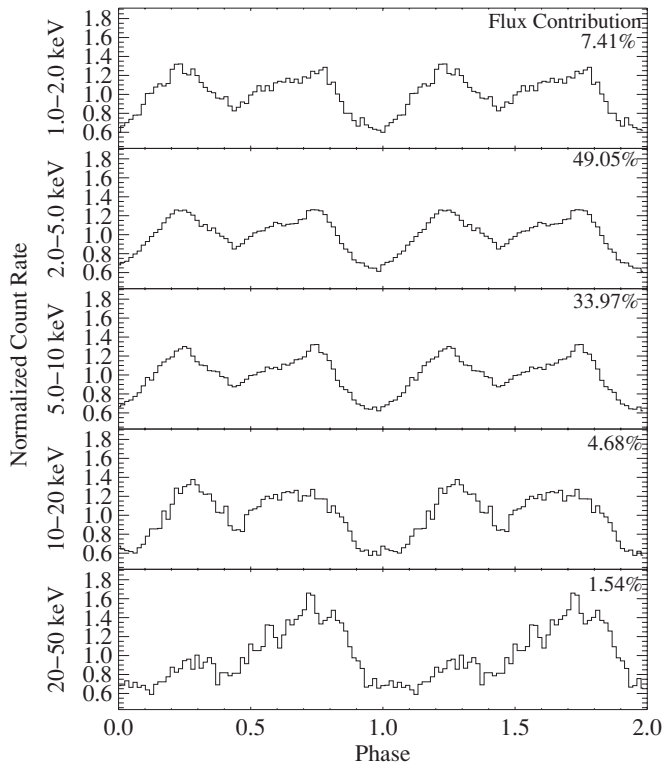


Figure 6. Energy-resolved pulse profiles for the co-added XIS and PIN data from 2006. Flux contributions are listed for each energy band, representing the percentage of the total flux contributed by that energy range.

the length of the pulse period. Nevertheless, these numbers are consistent with the trends in the pulse period seen by both Fritz et al. (2006) and Inam et al. (2009). The long-term evolution of the pulse period is shown in Figure 5 with the two *Suzaku* observations falling in the midst of the second torque reversal, restoring the source to its previous long-term spin-down rate (Inam et al. 2009). Physical implications of this event will be discussed in Section 6.

Using these periods, we generated pulse profiles for each observation. The profiles are shown in Figures 6 and 7, exhibiting a double peak with the initial peak being much weaker in the higher energy bands.

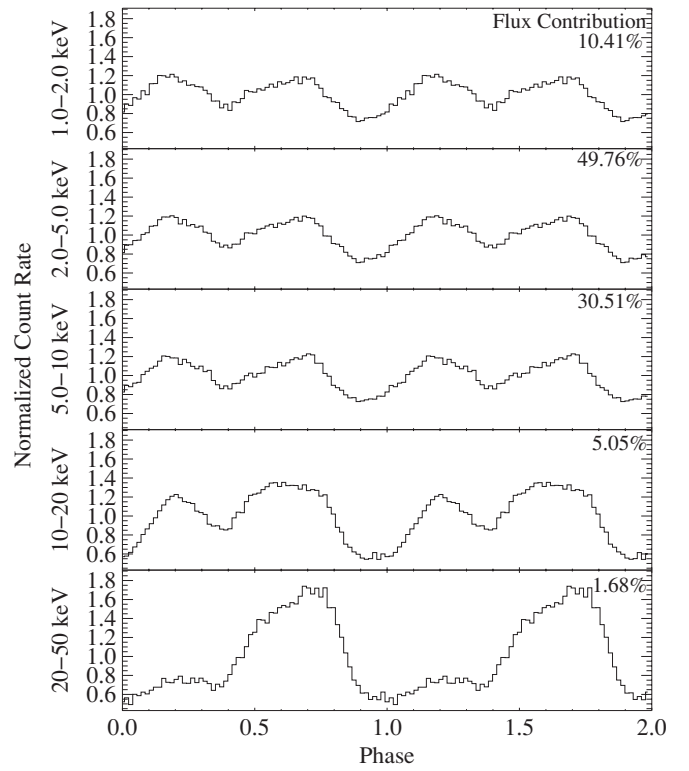


Figure 7. Energy-resolved pulse profiles for the co-added XIS and PIN data from 2007. Flux contributions are listed for each energy band, representing the percentage of the total flux contributed by that energy range.

4.2. Phase-resolved Spectral Analysis

We divided the pulse profiles into six regions as shown in the first sections of Figures 8 (2006) and 9 (2007) and extracted spectra for each region separately. Each bin had an average good exposure time per XIS of 9.5 ks for 2006 and 13.2 ks for 2007. The number of bins was chosen as a trade-off between achieving good time or phase resolution and having adequate signal to noise within each subspectrum. We applied the best-fit time-averaged FDCut models, allowing the following parameters to be free: the power-law photon index (Γ), the power-law normalization, the cutoff energy, the CRSF energy and depth, the Fe line intensity, and the 10 keV bump energy and depth. Other parameters were kept fixed in the fits at their time-averaged values; for some, such as the e -folding energy, there was no evidence of variability when these parameters were left free; thus we kept these parameters fixed to minimize any potential systematic effects on other free parameters. The iron line energies and widths were also kept fixed since we do not expect them to vary with phase. The results for selected model parameters are plotted in Figures 8 (2006) and 9 (2007). We caution, however, that with a low number of pulse bins, evidence for variation in these parameters as well as correlation with flux is not highly robust.

For both sets of data we find that the folding energy does not exhibit strong evidence of variation over the pulse phase. The cutoff energy and Γ do seem to vary over the phase, with both parameters reaching high values in bins 0 and 5 and minimum values near bins $\sim 2-4$. The Fe line depth shows some variation over the pulse with minimum values in the largest dip. There also seem to be small variations in the CRSF parameters, all of which reach their largest values during the first pulse peak. However, the low number of counts above 10 keV during the

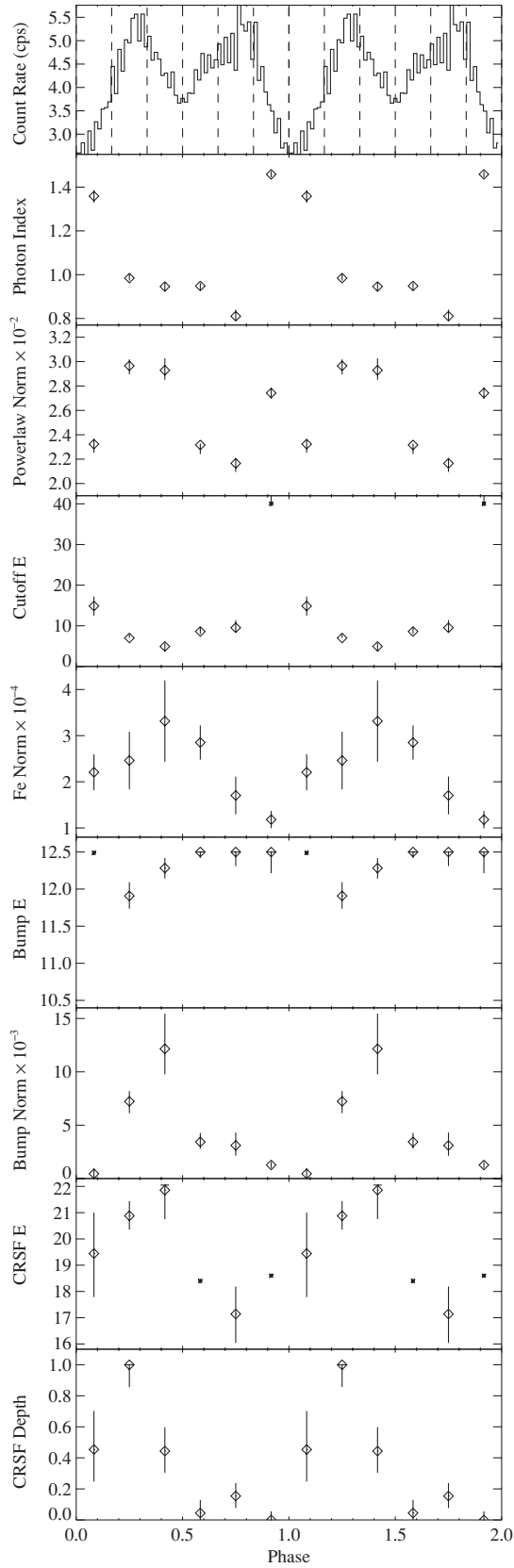


Figure 8. Results for phase-resolved spectral fitting for 2006. The pulse profile is for XIS0. For units see Table 1. A star symbol (*) indicates that the energy is unconstrained because the component is not needed for good fit. The CRSF depth is capped at 1.0 and the 10 keV bump feature energy is capped at 12.5 keV in order to avoid degeneracy between these two components.

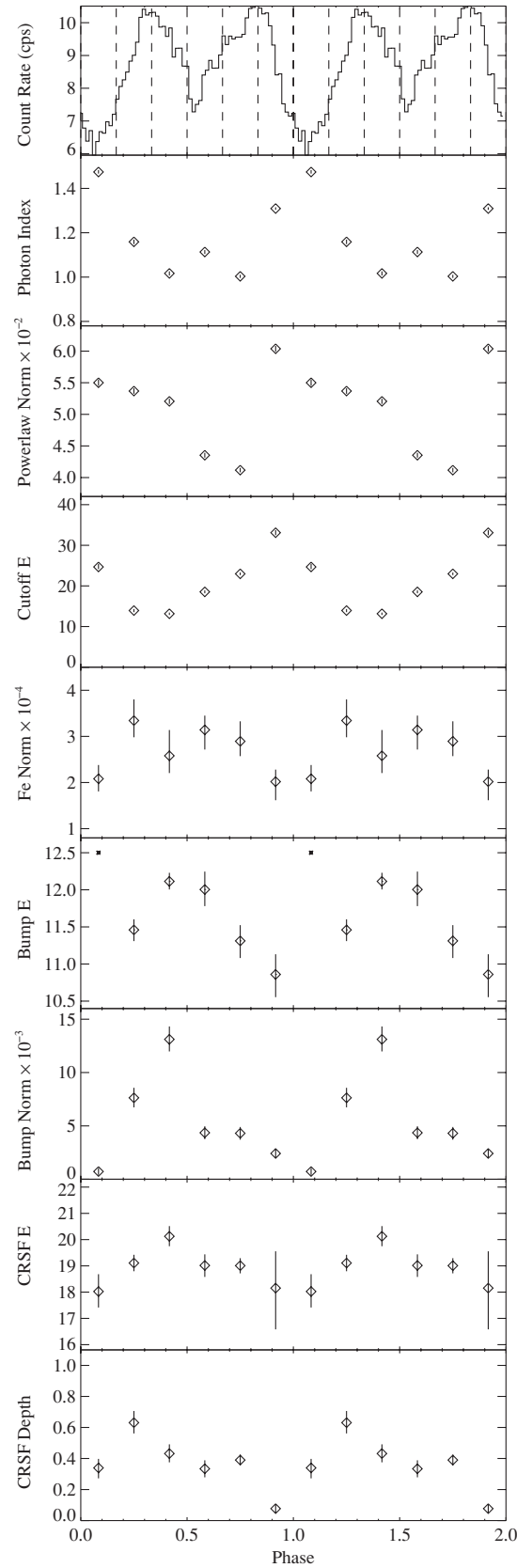


Figure 9. Results for phase-resolved spectral fitting for 2007. The pulse profile is for XIS0. For units see Table 1. A star symbol (*) indicates that the energy is unconstrained because the component is not needed for good fit.

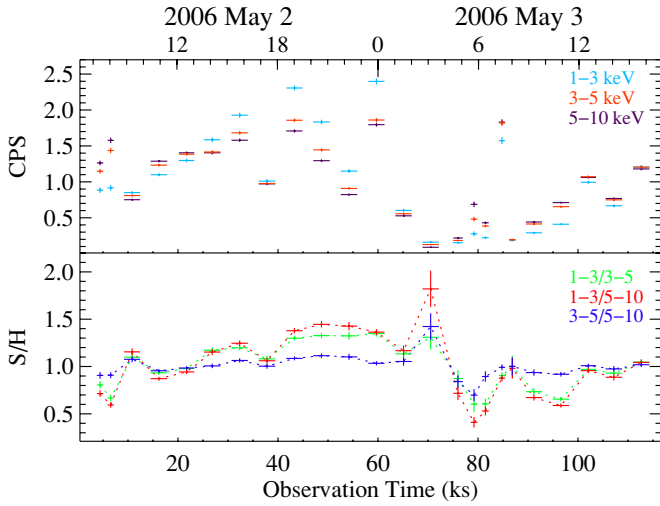


Figure 10. Energy-resolved, background-subtracted, light curves, and softness ratios from XIS0 for 2006.

(A color version of this figure is available in the online journal.)

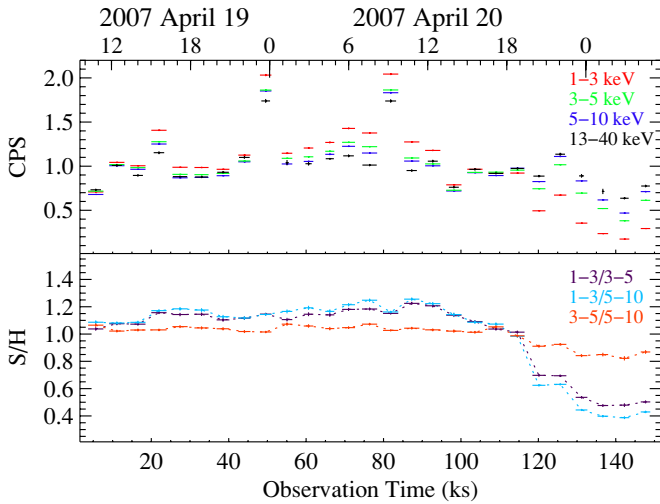


Figure 11. Energy-resolved, background-subtracted, light curves, and softness ratios from XIS0 for 2007.

(A color version of this figure is available in the online journal.)

first peak and the influence of the parameters of the 10 keV feature produce a lack of robustness in this result. The fit results also suggest that the properties of the 10 keV feature may vary as a function of pulse phase, but as we cautioned earlier, there may be systematic effects hampering our ability to measure the properties of this feature accurately.

5. TIME-RESOLVED SPECTROSCOPY

For a preliminary exploration of spectral variability as a function of time, we present count rate light curves binned on the timescale of the satellite orbit in Figures 10 (2006) and 11 (2007). Softness ratios are also shown, including (1–3)/(3–5) keV, sensitive to variations in N_H , and (3–5)/(5–10) keV, sensitive to variations in Γ . Additionally, Figures 12 and 13 show hardness ratios plotted against each other for each interval. The observational data points in these color–color plots were obtained adding data from XIS0 and XIS3, while the grids were created by deriving colors from simulated spectra. The latter are based on the spectral parameters of the point with the highest value of 1.5–3 keV over 3–10 keV (excluding points from the dips and flares) and allowing for an additional absorp-

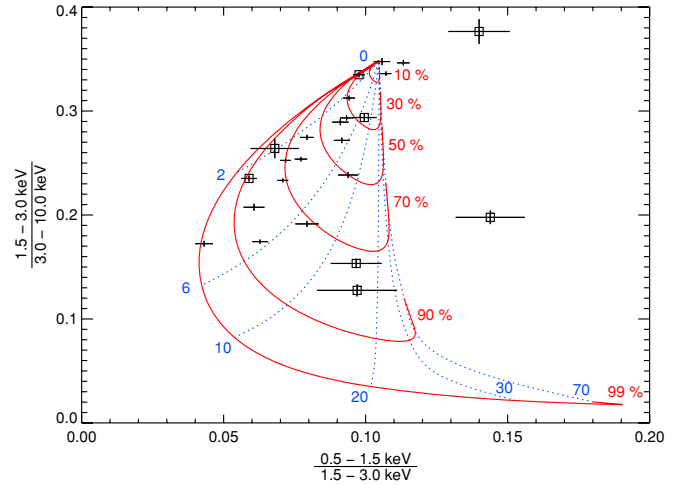


Figure 12. Color-color diagram for the 2006 observation with a partial covering grid where solid lines are covering fraction contours and dotted lines show constant N_H . Boxed data points correspond to the deep dip between ~ 60 ks and 100 ks and do not fit on the partial covering grid.

(A color version of this figure is available in the online journal.)

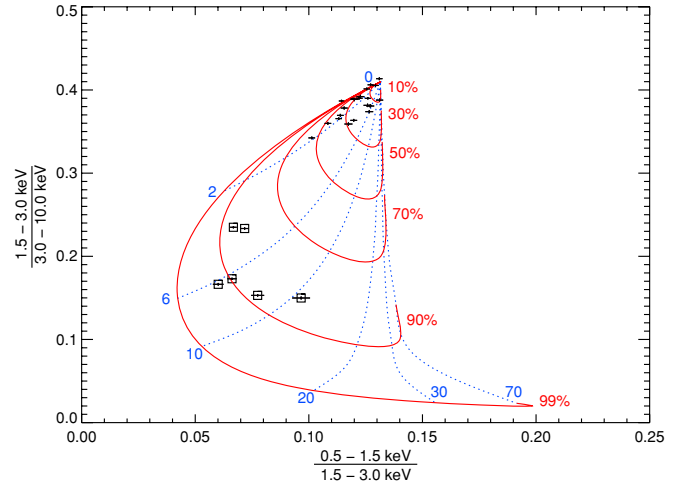


Figure 13. Color-color diagram for the 2007 observation with a partial covering grid where solid lines are covering fraction contours and dotted lines show constant N_H . Boxed points correspond to the dip in the last ~ 40 ks of the observation and are consistent with a partial cover.

(A color version of this figure is available in the online journal.)

tion component, partially covering the X-ray source, i.e., the “pcfabs” component in XSPEC. Using the response matrices for XIS0 and XIS3, hardness ratios for a grid of values of the covering fraction and the additional N_H were calculated and then interpolated to create the solid and dotted lines in Figures 12 and 13.

For the 2006 observation, the softness ratios vary over time, beginning and ending hard, while softening in the middle, suggesting that N_H is varying over the observation. The prolonged dip in 2006 between 60 ks and 100 ks shows an interesting behavior, beginning very soft but then hardening quickly. These points are shown in Figure 12 as squares and clearly do not lie along the partial covering grid, indicating that this dip is not caused by a dramatic increase in N_H . Together with the softness at the beginning of the dip, this implies a variation in Γ and that the cause of the dip is not absorption but is primarily associated with the continuum component. For the 2007 observation, the (1–3)/(3–5) keV softness ratio light curve exhibits a dip during the last ~ 40 ks of the observation, suggesting an increase in N_H ,

possibly caused by, for example, a relatively dense clump of material traversing the line of sight. These dip points (indicated by squares in Figure 13) are consistent with a high density partial covering material in the line of sight. The (3–5)/(5–10) keV softness ratio light curve is roughly constant, suggesting that Γ does not strongly vary, except possibly toward the final ~ 20 ks.

We divided the 2006 and 2007 data into 6 and 14 bins respectively, trying to ensure enough counts in each bin to make spectral fitting possible, resulting in each bin having an average good exposure time of roughly 11 ks (2006) or 5 ks (2007). The significant difference in binning for the two observations stems from the extended dip in 2006 (see the top panel of Figure 14), which caused the average flux to be ~ 2.5 times fainter than 2007. We applied the best-fit time-averaged FDCut models, keeping the iron line energies and widths, the 10 keV feature energy and width, and the e -folding energy fixed at the time-averaged value. The light curves and selected model component parameters are plotted in Figures 14 (2006) and 15 (2007).

In both observations, we note that the Fe line depth is strongly correlated with the flux. Correlation coefficients were found to be 0.86 for 2006 and 0.95 for 2007 with null-hypothesis probabilities of 97% and $>99.99\%$, respectively. The implications for the geometry of the Fe-line-producing material around the source will be discussed in Section 6.

For the 2006 observation we do see some variation in N_H and Γ , particularly during the dip between 60 and 100 ks. Two-dimensional contour plots of N_H versus Γ calculated with the cutoff energy left as a free parameter for the lowest flux subspectrum show no strong correlation between the two parameters; additionally, Monte Carlo simulations show a distribution in parameter values only on scales similar to the calculated error bars which are very small compared to the observed parameter variations. Standard deviations for N_H and Γ were 0.02 cm^{-2} and 0.015 , respectively. In addition, we investigated possible correlations between Γ and the cutoff energy in the low flux states but again, two-dimensional contour plots and Monte Carlo simulations indicated that the degree of correlation was much smaller than the observed variation.

For the 2007 observation, there is a doubling in N_H during the final 2–3 spectra, from $\sim 2 \times 10^{22}$ to $\sim 4 \times 10^{22} \text{ cm}^{-2}$. Through most of the observation Γ is roughly constant, but then it too changes in the final three spectra, flattening significantly where the flux reaches its lowest values. Contour plots of Γ as a function of N_H for the final three spectra yielded no evidence for any strong degeneracy between these two parameters from one time bin to the next (Figure 16). It is possible, however, that the dip in Γ may actually be a result of not using a partial covering model for the absorber, since we see in Figure 13 that the dip is consistent with partial covering. The cutoff energy also decreased during this time, but we caution that there may be systematic effects associated with the lowest flux levels. There is no strong evidence for variation in the parameters of the CRSF or the 10 keV bump energy and width; however, the 10 keV bump normalization appears to track the continuum flux, consistent with this feature being a part of the emission continuum we do not yet fully understand.

6. DISCUSSION

6.1. Properties of the CRSF

Observations of CRSFs allow direct measurement of the neutron star's magnetic fields, as the line energy $E_{\text{cyc}} \propto B/(1+z)$, where z is the gravitational redshift of the line-forming region.

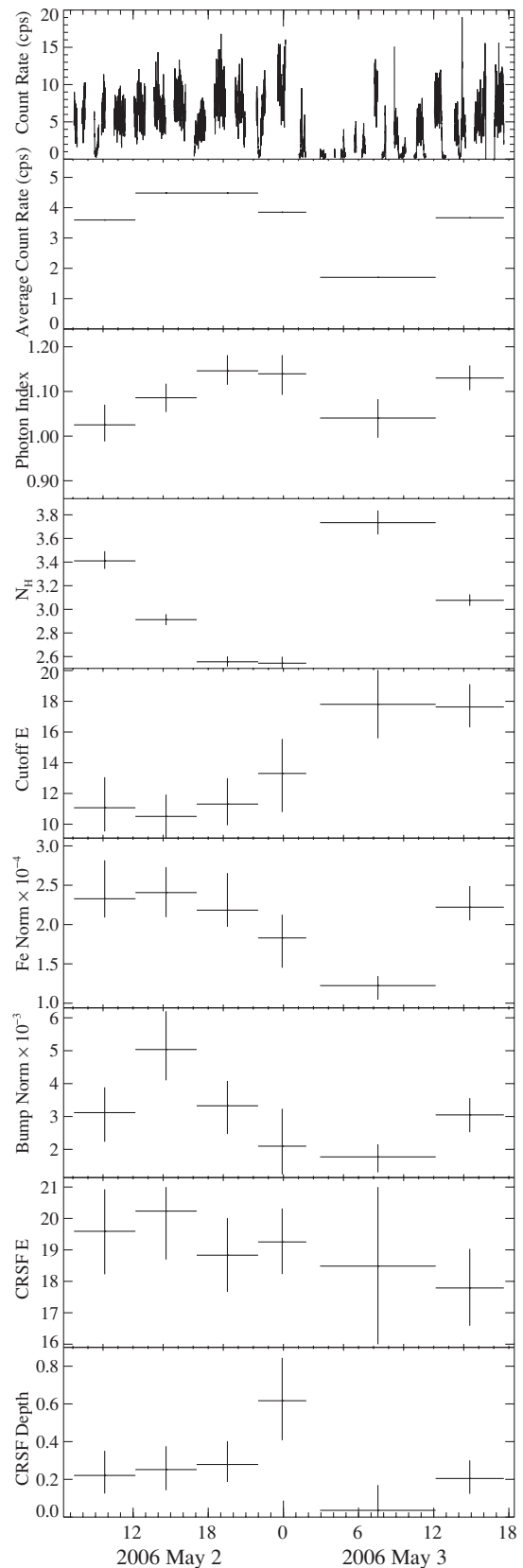


Figure 14. Spectral fitting over time for 2006. The light curve shown is for XIS0. For units see Table 1.

Their properties (depths, profiles, etc.) depend on the pulsar X-ray emission processes and the behavior of matter in strong magnetic fields (Meszaros & Nagel 1985). CRSFs thus carry a wealth of information about the environment in which they are

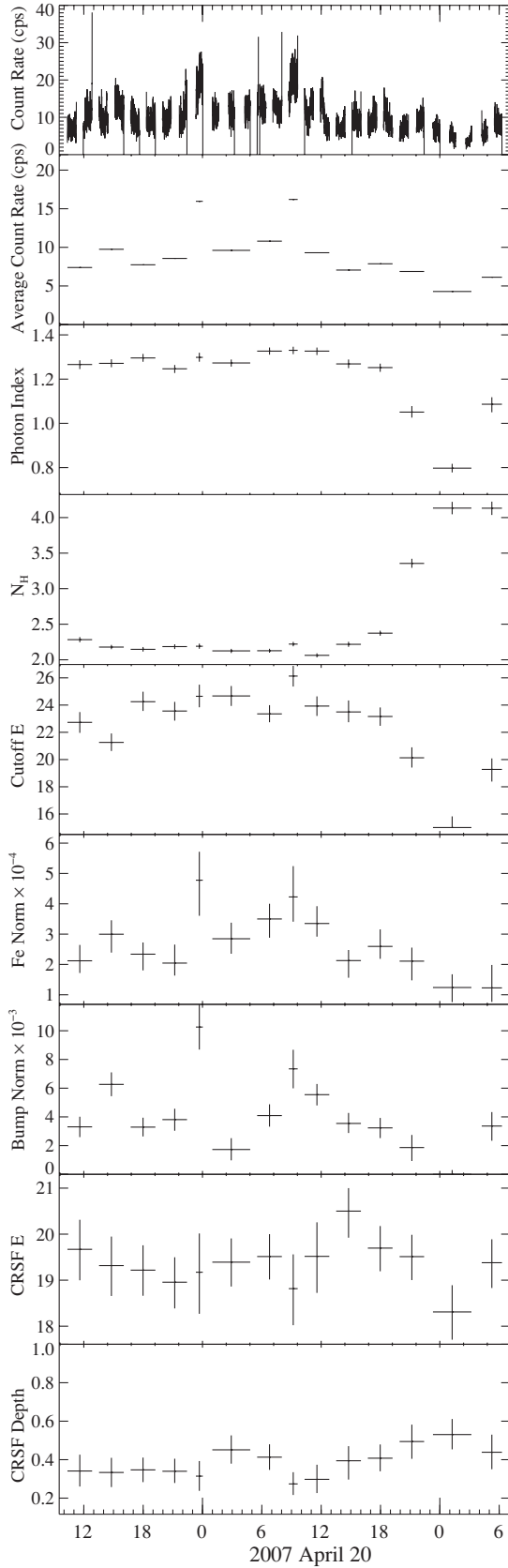


Figure 15. Spectral fitting over time for 2007. The light curve shown is for XIS0. For units see Table 1.

produced. For 4U 1907+09, we measure the energy centroid of the CRSF to be consistent with previous measurements, e.g., that of Cusumano et al. (1998) who calculated a magnetic field

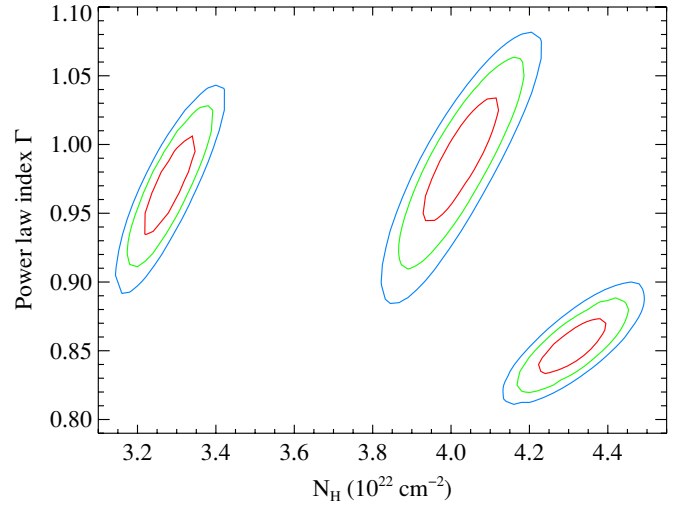


Figure 16. Contour plots of N_H vs. Γ for the last three time bins of the 2007 time-resolved spectra.

(A color version of this figure is available in the online journal.)

of $\sim 2.1 \times 10^{12}$ G using a value of $(1+z)^{-1} = 0.76$. The depth and width are also consistent with previous measurements.

In recent years, it has been discovered that in most accreting neutron stars the cyclotron line energy depends on the source flux (Mihara et al. 2004, 2007; Nakajima et al. 2006). Prominent recent examples for such a variability are V0332+53 and 4U 0115+63, where the cyclotron line energy *decreases* with flux (Mowlavi et al. 2006; Tsygankov et al. 2006; Nakajima et al. 2006) and Her X-1, where the line energy *increases* with flux (Staubert et al. 2007). The most prominent counterexample is A0535+262, where the line does not show any flux dependence (Caballero et al. 2007). The line variability can be understood by considering that for many accreting neutron stars, even though the overall source luminosity is only at a few percent of Eddington, the radiation field produced in the accretion column is close to or above the *local* Eddington limit. In this case, the accretion stream is rapidly decelerated by radiation pressure from the magnetic poles leading to a radiative shock, close to which the cyclotron lines are formed (Becker & Wolff 2005, 2007). The location of the shock depends on the ram pressure of the accretion stream and on the luminosity, L . For L close to the local Eddington luminosity, with increasing L the shock moves away from the neutron star, where the B -field is weaker. Thus the CRSF moves to lower energies, as is indeed observed in most sources. For smaller L , however, the ram pressure of the accreting material becomes important. As shown by Staubert et al. (2007) for the case of Her X-1, once L is below a critical luminosity the height of the column decreases as \dot{M} (and L) increases, because the accreted material “squeezes” the accretion mound. In this regime, therefore, the cyclotron line energy increases with luminosity. 4U 1907+09, however, is more like A0535+262, with no observed correlation between the CRSF energy and total flux. This could imply that it is somewhere between the two regimes described above.

We see strong variations in the CRSF parameters over the pulse phase, as well as in the continuum parameters, particularly E_{cutoff} and Γ . These clearly indicate that with a change in viewing angle we see different aspects of the accretion column structure. For details on phase-resolved pulsar spectra, see Coburn et al. (2002).

6.2. The Pulse-period Evolution

As seen in Section 4, 4U 1907+09 has an interesting and, as it turns out, rather unique pulse-period history. Typical X-ray binaries (XRBs) tend to maintain a trend of either spin-up or spin-down with short, intense episodes of the contrary superimposed (Bildsten et al. 1997). Examples of such behavior include Her X-1, Cen X-3, Vela X-1, and X Per. These shorter episodes are often interpreted to be due to short-term variations in the mass transfer rate from the donor star which give rise to short-term torque fluctuations (Ghosh & Lamb 1979). Such changes are always accompanied by large magnitude changes in L . The model used to describe this behavior is a magnetic coupling between the neutron star and its truncated accretion disk which transfers angular momentum to the neutron star, the accreted matter producing a torque and giving rise to non-zero values of \dot{P} (see, e.g., Ghosh et al. 1977, and references therein).

There are only three sources known to show a very different behavior: the LMXB GX 1+4, the ultracompact low-mass X-ray binary (LMXB) 4U 1626–67, and 4U 1907+09, all three of which were historically characterized by nearly constant \dot{P} over decade long periods with no short-term fluctuations but rare dramatic reversals of \dot{P} (Chakrabarty et al. 1997a, 1997b; Bildsten et al. 1997; Fritz et al. 2006). Monitoring of GX 1+4 by the *Fermi* Gamma-ray Burst Monitor shows it continuing in its new trend;⁶ however, 4U 1626–67 has shown another torque reversal (Camero-Arranz et al. 2009), returning to a spin-up trend after 18 yr of spin-down. Despite the difference of HMXB versus LMXB, 4U 1907+09 and 4U 1626–67 have shown very similar pulse-period behavior, both with $|P/\dot{P}| \sim$ several 1000 yr, neither showing any change in X-ray luminosity during reversals of \dot{P} , and both displaying similar P/\dot{P} ratios for their spin-up and spin-down periods.

With the simple magnetic torquing model outlined above, both the long distinct episodes of constant \dot{P} and the magnitude and sign of \dot{P} are difficult to explain together (Fritz et al. 2006, and references therein). As was observed in GX 1+4 (Chakrabarty et al. 1997b), one would expect dramatic changes in luminosity to accompany any torque reversal. No such correlation has been seen in either 4U 1626–67 or 4U 1907+09. Furthermore, it is difficult to understand why the torquing in the spin-up regime has a similar magnitude but reversed sign than in the spin-down regimes.

Recently, Perna et al. (2006) presented a new model in which torques can change without having to invoke retrograde disks or fluctuations in \dot{M} . This oblique rotator model can account for all observed properties of the spin history of 4U 1626–67, including the large values of $|P/\dot{P}|$ before and after the torque reversal and the virtually unchanged luminosity of the source. However, its prediction that such torque reversals must be very rare is contradicted by the second observed reversal of 4U 1907+09 in only a few years. Further monitoring of the pulse period will be needed as the evolution of the period of 4U 1907+09 may help to improve models of the accretion mechanism in XRBs.

6.3. The Fe lines and the Absorbing Gas: Tracing the Accretion Flow

We have studied the Fe K emission complex in detail, resolving the Fe $K\alpha$ line, detecting Fe $K\beta$ for the first time in this object, and detecting a strong Fe K edge at 7.11 keV

which we model employing an Fe abundance 4 times the solar value in the absorbing material.

It is possible that the same material that absorbs the X-ray continuum below 2 keV along the line of sight is responsible for transmitting the fluorescent emission lines. We can assume for simplicity that the absorbing gas is situated in an optically thin, uniform-density, spherical shell of material surrounding the central X-ray source. We can thus use Equation (4) of Yaqoob et al. (2001; based on Krolik & Kallman 1987), which yields an estimate for the equivalent width, EW_{calc} , of the Fe $K\alpha$ line given the photon index of the underlying continuum, the column density N_H , assumed Fe abundances, and a covering fraction f_c of the sky as seen from the central X-ray source.

With the abundances of Wilms et al. (2000), solar abundance for Fe means 2.69×10^{-5} Fe atoms for every H atom. We see that for the material obscuring 4U 1907+09, the Fe abundance is ~ 4 times this value. Using the best-fit values of Γ (1.15) and N_H ($2.18 \times 10^{22} \text{ cm}^{-2}$) from the 2007 time-averaged FDCut fit, we find $EW_{\text{calc}} = 47 \text{ eV} \cdot f_c$. With an observed EW of $47 \pm 4 \text{ eV}$, we can conclude that the Fe $K\alpha$ line is consistent with being transmitted by the absorbing material if the covering fraction is close to unity. It is thus likely that the absorbing material along the line of sight is in the stellar wind in the vicinity of the pulsar. The high covering factor implied for the Fe-line emitter, the lack of continuum emission observed below 1 keV in the time-averaged spectrum, and the absorbing/Fe-line emitting material being full-covering are all consistent with a wind-accreting geometry, as opposed to a disk-accreting geometry.

The Fe $K\alpha$ line energy, the $K\beta/K\alpha$ intensity ratio, and the properties of the absorber (e.g., edge consistent with neutral Fe K) all suggest that the bulk of the absorbing/Fe-line transmitting material is neutral or at most moderately ionized. Theoretical calculations based on Kallman & McCray (1982), however, indicate that the stellar wind should be fully ionized at the radius of the neutron star. According to Kallman & McCray, iron becomes fully ionized above $\log \xi = 3$, where $\xi \equiv L/nR^2$. Using the stellar wind parameters from Cox et al. (2005), we can calculate the ionization parameter, $\log \xi = 3.9$, indicating full ionization. We calculate the distance from the companion star at which the ionization of the wind is consistent with the observed emission features to be roughly 16 times the orbital radius of the pulsar. The existence of neutral, line-emitting iron close to the neutron star in the midst of a highly ionized wind could be possible if the wind from the companion star is clumpy rather than homogeneous. Sako et al. (1999) used the clumpy wind model to reconcile the presence of fluorescent lines in the spectrum of the HMXB Vela X-1 by considering an inhomogeneous wind with cool, dense clumps of neutral or near-neutral material. We will show in Section 6.4 using time variability arguments that this model is likely for the accretion in 4U 1907+09.

6.4. Variability of the Continuum Emission and Absorbing Components

Time-resolved spectral modeling shows that variations in the power-law component are observed in the 1–40 keV continuum variability. The multi-band light curves show correlated flux variations up to 10 keV, in agreement with this notion. Given the low column density, variations due to the absorbing material cannot account for continuum variability above 3 keV, particularly in the prolonged dip in the 2006 observation and the flares in the 2007 observation; though as noted earlier, the change in Γ coinciding with the dip at the end of the 2007 observation may

⁶ <http://gamma-ray.msfc.nasa.gov/gbm/science/pulsars/>

be due to incomplete modeling of a partial-covering absorber as indicated in Figure 13.

The X-ray continuum in wind-accreting pulsars is generally thought to originate in the accretion column as the accretion flow is channeled by the neutron star's magnetic fields onto its poles and then is decelerated in a radiative shock and settles onto the surface of the neutron star. Recent models attribute the X-ray emission to inverse Comptonization of soft seed photons (originating in the accretion mound and the shock front) as the photons interact with the compressing gas (e.g., Becker & Wolff 2007). Variations in Γ could thus indicate changes in the optical depth, temperature, or geometry and therefore the average number of upscatterings a typical photon undergoes.

Finally, the observation of a doubling in N_H during the final ~ 30 ks of the 2007 observation further indicates that the absorbing material is indeed clumpy. According to recent calculations, winds of O and B stars show strong clumping, due to instabilities in the line-driven acceleration mechanism (Dessart & Owocki 2005). Oskinova et al. (2007) confirmed this result, showing that clumping is indeed necessary to reconcile measured line strengths with observed mass loss rates of the companion star. Observationally, in the HMXB Vela X-1, a system similar to 4U 1907+09, Sako et al. (1999) showed that a clumpy wind is required to explain the lines seen in the *Chandra* gratings spectrum. This result was confirmed in a statistical analysis of the Vela X-1 flaring behavior (Fürst et al. 2008), who found typical clump masses around 2.3×10^{20} g.

Flares seen in 4U 1907+09 on the scale of ~ 1 hr as in our 2007 observation are consistent with flaring behavior described by Owocki et al. (2009) and Walter & Zurita-Heras (2007). Based on the clumpy wind models, Walter & Zurita-Heras calculated clump masses from the brightness and duration of typical flares. Their results are on the order of 10^{21} g with N_H values for the clumps around 10^{22} cm $^{-2}$. Using similar methods we obtain clump masses of around 1.5×10^{20} g and a value for N_H also around 10^{22} cm $^{-2}$. Additionally, this value for N_H is consistent with the dip in the 2007 observation where the increase in N_H is about 2×10^{22} cm $^{-2}$ which could be caused by a clump passing through the line of sight.

From the color-color diagrams we can see that the dip in the 2007 observation and the overall dimness of the 2006 observation are consistent with a partial covering absorber in the line of sight. This could be caused by the clumps in the stellar wind partially obscuring the object. The prolonged dip in the 2006 observation does not fit this explanation; however it can still be explained by a clumpy wind model. Since clumpy winds are expected to have regions where the wind density is significantly below its average density, this would explain dips due to sudden decreases in the mass accretion rate as in 2006 and previously observed in 4U 1907+09 by in't Zand et al. (1997). The clumpy wind model therefore explains the observed dipping and flaring behavior as well as the presence of near-neutral iron in the otherwise highly ionized stellar wind.

7. CONCLUSIONS

The use of the *Suzaku* observatory for our two observations has led to several advantages over previous observations of 4U 1907+09 in that the broadband coverage of the XIS+PIN has allowed us to probe in depth the spectral variability in this source. The XIS offers CCD resolution and a high effective area to study Fe K bandpass features, plus higher sensitivity below 3 keV than previous investigations to accurately quantify absorption. The PIN has very low background covering the

13–40 keV band, allowing us to analyze characteristics of the CRSF at 19 keV.

Simultaneous multi-band dips and flares are likely caused by changes in accretion rate possibly due to inhomogeneous, clumpy winds. Dips in the soft band could also be explained by clumpy winds when a clump passes through the line of sight.

We have studied the Fe K α line with unprecedented precision and the Fe K β line for the first time. We have determined that the iron-line emitting material is very close to the pulsar and therefore could also be due to cooler, denser clumps in an otherwise fully ionized stellar wind.

The pulse period has undergone dramatic changes recently and we are able to fill in the gap between Fritz et al. (2006) and Inam et al. (2009) where the second torque reversal took place. The torque reversals cannot be fully explained by any current model.

Finally, we have observed the CRSF at ~ 19 keV in our time-averaged, phase-resolved, and time-resolved spectral fitting. Lack of variation of the cyclotron line energy with flux places 4U 1907+09 in the same regime as A0535+262, somewhere in between the large and small luminosity regimes where perhaps the effect of the ram pressure is just enough to keep the shock front of the accretion column at a fairly constant height.

This research has made use of data obtained from the *Suzaku* satellite, a collaborative mission between the space agencies of Japan (JAXA) and the USA (NASA). This work has made use of HEASARC online services, supported by NASA/GSFC. The research was supported by NASA contract NAG5-30720, and grants NNX08AC88G and NNX09AG79G. We acknowledge support from the Bundesministerium für Wirtschaft und Technologie under Deutsches Zentrum für Luft- und Raumfahrt grants 50OR0701, 50OR0808, and 50OR0905. F.F. acknowledges support from a Deutscher Akademischer Austauschdienst stipend.

REFERENCES

- Arnaud, K. 1996, in ASP Conf. Ser. 101, *Astronomical Data Analysis Software and Systems*, ed. G. Jacoby & J. Barnes (San Francisco, CA: ASP), 17
- Baykal, A., Inam, ç., Ali Alpar, M., in't Zand, J. J. M., & Strohmayer, T. 2001, *MNRAS*, **327**, 1269
- Baykal, A., Inam, S. C., & Beklen, E. 2006, *MNRAS*, **369**, 1760
- Becker, P. A., & Wolff, M. T. 2005, *ApJ*, **630**, 465
- Becker, P. A., & Wolff, M. T. 2007, *ApJ*, **654**, 435
- Bildsten, L., et al. 1997, *ApJS*, **113**, 367
- Boldt, E. 1987, in Proc. IAU Symp. 124, *Observational Cosmology* (Dordrecht: Reidel), 611
- Caballero, I., et al. 2007, *A&A*, **465**, L21
- Camero-Arranz, A., Finger, M. H., Ikhsanov, N. R., Wilson-Hodge, C. A., & Beklen, E. 2009, arXiv:0906.4224
- Chakrabarty, D., Roche, P., van Kerkwijk, M. H., & Larkin, J. E. 1997a, *BAAS*, **29**, 840
- Chakrabarty, D., et al. 1997b, *ApJ*, **481**, L101
- Coburn, W., et al. 2002, *ApJ*, **580**, 394
- Cox, N. L. J., Kaper, L., & Makiem, M. R. 2005, *A&A*, **436**, 661
- Cusumano, G., et al. 1998, *A&A*, **338**, L79
- Dessart, L., & Owocki, S. P. 2005, *A&A*, **437**, 657
- Fritz, S., Kreykenbohm, I., Wilms, J., Staubert, R., Bayazit, F., Pottschmidt, K., Rodriguez, J., & Santangelo, A. 2006, *A&A*, **458**, 885
- Fukazawa, Y., et al. 2009, *PASJ*, **61**, 17
- Fürst, F., Kreykenbohm, I., Wilms, J., Kretschmar, P., Klochkov, D., Santangelo, A., & Staubert, R. 2008, Proc. 7th INTEGRAL Workshop, <http://pos.sissa.it/cgi-bin/reader/conf.cgi?confid=67>
- Ghosh, P., & Lamb, F. K. 1979, *ApJ*, **234**, 296
- Ghosh, P., Pethick, C. J., & Lamb, F. K. 1977, *ApJ*, **217**, 578
- Giacconi, R., et al. 1971, *ApJ*, **165**, L27
- Inam, S. ç., Sahiner, S., & Baykal, A. 2009, *MNRAS*, **395**, 1015

- in't Zand, J. J. M., Baykal, A., & Strohmayer, T. E. 1998, [ApJ](#), **496**, 386
- in't Zand, J. J. M., Strohmayer, T. E., & Baykal, A. 1997, [ApJ](#), **479**, L47
- Kallman, T. R., & McCray, R. 1982, [ApJ](#), **50**, 263
- Krolik, J. H., & Kallman, T. R. 1987, [ApJ](#), **320**, L5
- Leahy, D. A., et al. 1983, [ApJ](#), **266**, 160
- Maeda, Y., et al. 2008, JX-ISAS-SUZAKU-MEMO-2008-06
- Makishima, K., Kawai, N., Koyama, K., Shibazaki, N., Nagase, F., & Nakagawa, M. 1984, [PASJ](#), **36**, 679
- Makishima, K., Mihara, T., Nagase, F., & Murakami, T. 1992, in *Frontiers Science Ser. 2, Frontiers of X-Ray Astronomy*, Proc. 28th Yamada Conf., ed. Y. Tanaka & K. Koyama (Tokyo: Universal Academy Press), 23
- Makishima, K., Mihara, T., Nagase, F., & Tanaka, Y. 1999, [ApJ](#), **525**, 978
- Marshall, N., & Ricketts, M. J. 1980, [MNRAS](#), **193**, 7
- McBride, V. A., et al. 2006, [A&A](#), **451**, 267
- Meszáros, P., & Nagel, W. 1985, [ApJ](#), **298**, 147
- Mihara, T. 1995, Ph.D. thesis, Department of Physics, Univ. Tokyo
- Mihara, T., Makishima, K., & Nagase, F. 2004, [ApJ](#), **610**, 390
- Mihara, T., et al. 2007, [Prog. Theor. Phys. Suppl.](#), **169**, 191
- Mitsuda, K., et al. 2007, [PASJ](#), **59**, 1
- Mowlavi, N., et al. 2006, [A&A](#), **451**, 187
- Nagel, W. 1981, [ApJ](#), **251**, 288
- Nakajima, M., Mihara, T., Makishima, K., & Niko, H. 2006, [Adv. Space Res.](#), **38**, 2756
- Oskinova, L. M., Hamann, W.-R., & Feldmeier, A. 2007, [A&A](#), **476**, 1331
- Owocki, S. P., Romero, G. E., Townsend, R. H. D., & Araudo, A. T. 2009, [ApJ](#), **696**, 690
- Palmeri, P., Mendoza, C., Kallman, T. R., Bautista, M. A., & Meléndez, M. 2003, [A&A](#), **410**, 359
- Perna, R., Bozzo, E., & Stella, L. 2006, [ApJ](#), **639**, 363
- Protassov, R., van Dyk, D. A., Connors, A., Kashyap, V. L., & Siemiginowska, A. 2002, [ApJ](#), **571**, 545
- Sako, M., Liedahl, D. A., Kahn, S. M., & Paerels, F. 1999, [ApJ](#), **525**, 921
- Schönherr, G., Wilms, J., Kretschmar, P., Kreykenbohm, I., Santangelo, A., Rothschild, R. E., Coburn, W., & Staubert, R. 2007, [A&A](#), **472**, 353
- Staubert, R., Shakura, N. I., Postnov, K., Wilms, J., Rothschild, R. E., Coburn, W., Rodina, L., & Klochkov, D. 2007, [A&A](#), **465**, L25
- Suchy, S., et al. 2008, [ApJ](#), **675**, 1487
- Takahashi, T., et al. 2007, [PASJ](#), **59**, 35
- Tanaka, Y. 1986, in *IAU Coll. 89, Radiation Hydrodynamics in Stars and Compact Objects*, ed. D. Mihalas & K.-H. A. Winkler (Heidelberg: Springer), 198
- Tsygankov, S. S., Lutovinov, A. A., Churazov, E. M., & Sunyaev, R. A. 2006, [MNRAS](#), **371**, 19
- Van Kerkwijk, M. H., van Oijen, J. G. J., & van den Heuvel, E. P. J. 1989, [A&A](#), **209**, 173
- Verner, D. A., Ferland, G. J., Korista, K. T., & Yakovlev, D. G. 1996, [ApJ](#), **465**, 487
- Walter, R., & Zurita Heras, J. 2007, [A&A](#), **476**, 335
- White, N. E., Swank, J. H., & Holt, S. S. 1983, [ApJ](#), **270**, 711
- Wilms, J., Allen, A., & McCray, M. 2000, [ApJ](#), **542**, 914
- Yaqoob, T., George, I. M., Nandra, K., Turner, T. J., Serlemitsos, P. J., & Mushotzky, R. F. 2001, [ApJ](#), **546**, 759